

Supporting Information

for

Nanocrystal Diffusion in a Liquid Thin Film Observed by *in situ* Transmission Electron
Microscopy

Haimei Zheng, Shelley A. Claridge, Andrew M. Minor, A. Paul Alivisatos*, Ulrich
Dahmen#

To whom correspondence should be addressed. * E-mail: alivis@berkeley.edu or #
Email: udahmen@lbl.gov

This file includes:

Materials and Methods

Supporting Text

Tables S1 to S3

Figs. S1 to S8

Movies S1 to S3

References

I. Materials and Methods

General information. Citrate coated 5, 10, and 15 nm gold particles with deviation less than 10% in diameter were purchased from Ted Pella (Redding, CA). The bis-(*p*-sulfonatophenyl)phenylphosphine (BSPP) dihydrate dipotassium ligand, which stabilizes the nanoparticles in high-salt buffers, was obtained from Strem Chemicals (Newburyport, MA). In all experiments, 15% (volume ratio) glycerol was added to the gold nanoparticle solutions in order to increase the viscosity and decrease the vapor pressure of the liquid. Nanoparticle sample concentration was carried out in a Fisher Centrifig 228 bench top centrifuge. UV-Vis absorption measurements were taken using a Perkin-Elmer Lambda 35 spectrometer.

Preparation of citrate-gold nanoparticles. 100 μL each of as-purchased citrate coated 5, 10 and 15 nm gold nanoparticles were mixed together and 53 μL glycerol was added to the mixture. The mixed solution was agitated for 15 min.

Preparation of BSPP-gold nanoparticles. BSPP-passivated gold nanoparticles were prepared using a previously published procedure described briefly here¹. 60 mg BSPP was added to 100 mL citrate coated gold nanoparticle solution. The mixture was stirred at room temperature overnight in order to allow phosphine ligands to replace the citrate ligands. Following overnight incubation, NaCl was added to the stirring mixture until a color change from red to cloudy purple was observed. The solution was transferred to 50 mL centrifuge tubes and centrifuged at room temperature for 10 min at 3500 rpm to collect the precipitated gold. The supernatant was removed, and the pellet resuspended in phosphine buffer (1 mg BSPP in 1 mL de-ionized water). Nanoparticles were quantified by measuring the absorbance at the wavelength of 520 nm and calculating the particle concentration using Beer's law, $A = \epsilon bc$, where A is the absorbance; ϵ is the extinction coefficient: $\epsilon_{520}(5 \text{ nm}) = 9.6 \times 10^6 \text{ M}^{-1}\text{cm}^{-1}$, $\epsilon_{520}(10 \text{ nm}) = 9.6 \times 10^7 \text{ M}^{-1}\text{cm}^{-1}$, and $\epsilon_{520}(15 \text{ nm}) = 3.6 \times 10^8 \text{ M}^{-1}\text{cm}^{-1}$; b is the path length of the cuvette in which the sample is contained, $b = 1 \text{ cm}$; c is the particle concentration. Concentrations of 3 μM for 5 nm Au particles, 1 μM for 10 nm particles, and 0.5 μM for 15 nm particles were achieved. 10 μL 5nm Au particles, 6 μL 10 nm particles and 12 μL 15 nm particles with the above concentrations were mixed, and 80 μL de-ionized water and 20 μL glycerol were added. The mixture was agitated gently for 15 min.

Liquid cell fabrication and sample loading for TEM A schematic of the liquid cell design is shown in Fig. S1. Cells were fabricated using ultra thin silicon wafers (100 μm , 4-inches, p-doped) purchased from Virginia Semiconductor (Fredericksburg, VA). The fabrication process includes growing low stress silicon nitride membranes on the silicon wafers (20 nm in thickness) followed by lithographic patterning, etching and bonding. The bottom and top pieces of the liquid cell were bonded together at 120 $^{\circ}\text{C}$ for 1h using a thin layer of indium. The indium layer was deposited on the bottom piece by following the process of lithographic patterning, indium deposition by sputtering, and lift-off. Indium acts as a spacer as well as the sealing material for the liquid cell. 100 nm indium spacing was used for the current experiments, although different thickness can be

achieved. All fabrication was conducted at the Microfabrication Lab of the University of California at Berkeley.

About 100 nL of liquid can be loaded into the cell. The liquid loading was facilitated by use of a syringe and Teflon nanotubes (purchased from Cole-Parmer, VH, IL) to control the size of droplets and a micromanipulator to precisely direct the droplets in the liquid reservoir without contaminating the electron transmission window.

The liquid cell has dimensions that allow it to fit into any standard TEM holder without modification. A JEOL 3010 TEM with a LaB6 filament operated at 300 keV was used. An electron current density of 700 A/m^2 was maintained during the experiments.

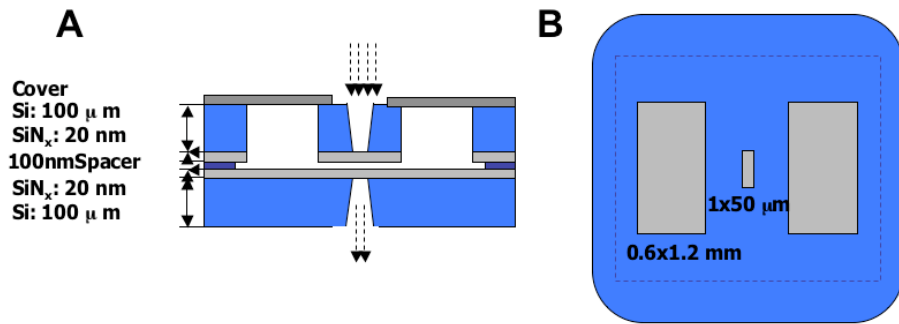


Fig. S1. A liquid cell schematic. **(A)** Cross-sectional view. **(B)** Planar-view. Lateral dimensions of the liquid cell: $2.6 \times 2.6 \text{ mm}$ and 3 mm in diagonal; reservoirs: $0.6 \times 1.2 \times 0.1 \text{ mm}$; the electron transparent window: $1 \times 50 \mu\text{m}$; cover: $0.6 \times 0.6 \text{ mm}$ for the hole and its outer dimensions are the same as the liquid cell.

II. Supporting Text

2.1 Liquid evaporation evaluation

The liquid inside the liquid cell slowly evaporates due to the imperfect seal conditions of the cell in a vacuum environment and a relative high vapor pressure of the liquid. It is possible that the electron beam contributes to the evaporation of the liquid. However, since liquid inside the liquid reservoirs also evaporates but is not exposed to the electron beam, we conclude that the electron beam does not make the main contribution to the liquid evaporation. Consequently, one side of the liquid film generally detaches from the silicon nitride membrane, creating a vapor-liquid interface. Liquid detaching from one side of the membranes was assumed based on the observations that the liquid sample was constantly changing the mass-thickness contrast (thinning in the liquid thickness) until drying patches formed (see advancing drying patches in Fig. S2) and eventually liquid was completely evaporated. In some cases, long distance particle movement dragged by the motion of detaching liquid was observed before the formation of drying patches.

The liquid evaporation rate was held at about 1 nm/min during the experiments, which was estimated by the total thickness of the liquid divided by the time it took to evaporate the liquid film. A linear evaporation rate was assumed^{S2}. In order to estimate the liquid thickness, the liquid cell was opened after the experiments and the thickness of indium spacer was measured by a profilometer. The thickness of the liquid film is assumed to be the same as the indium spacer. The evaporation rate was estimated for 20 liquid cell experiments under the same electron beam conditions (as seen above) and the average evaporation rate was 1 nm/min with a standard deviation of 0.5 nm/min. It should be noted that this is a rough estimate. Advanced measurement tools need to be developed for accurate measurements of liquid evaporation rate and the liquid thickness inside the liquid cell.

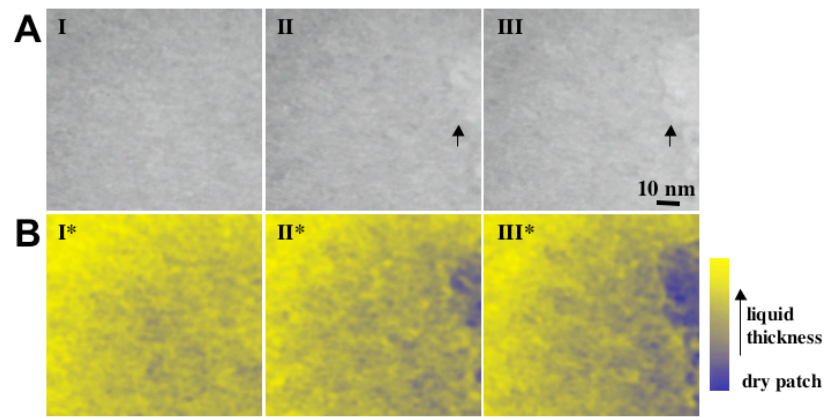


Fig. S2. Formation of drying patches in a liquid thin film. **(A)** An image sequence from the original recording. I. 0 s (arbitrary), II. 81 s and III. 94 s; Arrows highlight the advancing liquid-solid-vapor interface. **(B)** Color gradient maps (I*, II* and III*) corresponding to the images (I, II and III) in (A).

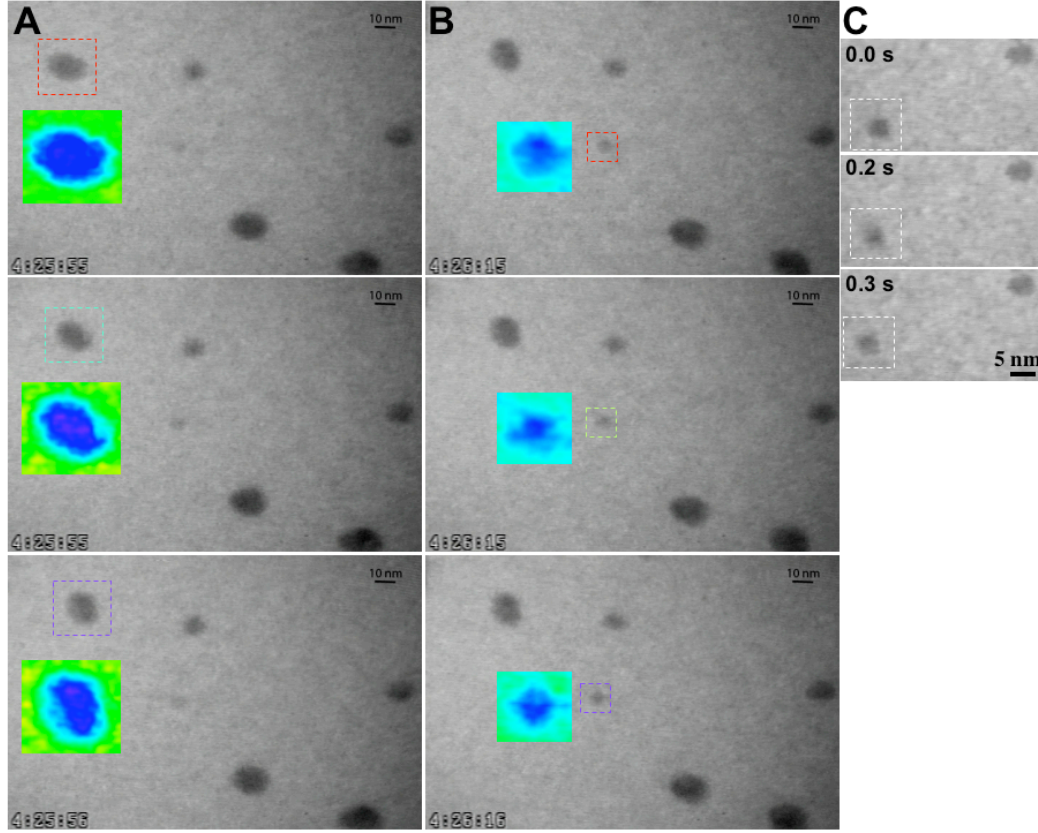


Fig. S3. Jump motion corresponding to particle orientation changes. The video images and enlarged color gradient maps of the selected areas showing the orientation changes of (A) a 5 nm particle and (B) a 15 nm particle during the jump. (C) Jumps corresponding to particle rolling (the selected particle) vs small-step movements showing no obvious changes in orientation (top right particle).

2.2 Electron beam effects

We consider the electron beam might have effects on the particle motion, including local heating, momentum transfer from the electron beam, and charging effects. We found that under our experimental set up with a low electron beam current density, such effects are negligible for the particle trajectory analysis. Below are the details of the analysis.

2.2.1 Estimation of temperature rise induced by electron beam irradiation

Estimation of electron energy loss

When the electron beam passes through a thin film material, the mean energy loss of the electrons can be estimated using the Bethe function^{S3}.

$$-\frac{dE(x)}{dx} = 2\pi N_0 q^4 \rho \frac{Z}{A} \frac{1}{E(x)} \ln\left(\frac{aE(x)}{I}\right), \quad (1)$$

where E is the electron energy, x is the distance along the path, Z and A are the average atomic number and gram atomic weight of the material, N_0 is Avogadro's number, q is the electronic charge, ρ is the density of the material, I is the mean excitation energy for energy loss in the material and can be estimated by $I=(9.76 + 58.8/Z^{-1.19})$ and a is constant with the value of 1.1658 for relativistic energy electrons.

The energy loss of the electron beam with an acceleration voltage of 300 keV passing through a few selected materials has been calculated, see the results in Table S1.

Table S1 Energy loss of electron beam (300keV) for different materials.

Materials	dE/dx(eV/nm)
Si ₃ N ₄	0.05
H ₂ O	0.041
Au	0.261

Electron beam induced temperature rise in a thin film

We assume all the energy dissipation from the electron beam transfers to heat. The heat dissipation mechanisms of an irradiated area in a two-dimensional thin film in a gas or fluid medium include radiation, convection and conduction through the medium and conduction through the film. In an ultra high vacuum, the heat conduction and convection through the vacuum is negligible. If we neglect the black body radiation, the heat dissipation of the irradiated area in a thin film in vacuum is mainly two-dimensional conduction through the film. The induced temperature rise of the irradiated area can be estimated using the heat conduction equation on a two-dimensional disk.

In a uniform thin film and steady-state, the two-dimensional heat conduction equation in cylindrical coordinates is given by:

$$-k \cdot \left(\frac{d^2 T}{dr^2} + \frac{1}{r} \frac{dT}{dr} \right) = J, \quad (2)$$

where k is thermal conductivity, the temperature distribution T is a function of radius r , J is heat flux density.

Firstly, we consider the heat transfer within the region of $R_1 \leq r < R_0$ (at R_0 , $T = T_{RT}$, room temperature, see Fig. S4A) and $J=0$. Equation (2) becomes:

$$\frac{d^2 T}{dr^2} + \frac{1}{r} \frac{dT}{dr} = 0. \quad (3)$$

Integration of equation (3) gives:

$$T = C_1 \ln r + C_2, \quad (4)$$

where C_1 , C_2 are constants. The following boundary conditions are applied.

$$\text{When } r=R_0, T= T_{RT}. \quad (5)$$

$$\text{When } r=R_1, dT/dr=C_1/R_1=Q/2\pi R_1 \cdot h \cdot k, \quad (6)$$

where Q is the total heat flux of the irradiated area, $Q=J_e \cdot \pi R_1^2 \cdot (dE/dX)$, J_e is the electron current density, h is the thickness of the film, and dE/dX is the total energy loss of per electron $dE/dX=(dE/dx) \cdot h$. Substituting (5) and (6) into (4), we get

$C_1 = -\frac{Q}{2\pi kh}$ and $C_2 = T_{RT} + \frac{Q}{2\pi kh} \ln R_2$. Applying C_1 and C_2 to equation (4) gives:

$$T = T_{RT} + \frac{Q}{2\pi kh} \ln \frac{R_2}{r}. \quad (7)$$

Therefore, when $r=R_1$, the temperature of the surface between the irradiated area and non-irradiated area of the film is given by

$$T_{R_1} = T_{RT} + \frac{Q}{2\pi kh} \ln \frac{R_0}{R_1}. \quad (8)$$

Secondly, we consider the temperature distribution within the irradiated area of $0 \leq r < R_1$, where there is a net constant power input from the electron beam, $J \neq 0$.

Integration of equation (2) gives

$$T = -\frac{1}{4k} Jr^2 + C_3 \ln r + C_4. \quad (9)$$

where C_3 and C_4 are constants. We apply the following boundary conditions.

When $r=0$, T is finite, therefore, $C_3=0$. When $r=R_1$, $T_{R_1} = T_{RT} + \frac{Q}{2\pi kh_0} \ln \frac{R_0}{R_1}$, therefore,

$C_4 = T_{R_1} + \frac{1}{4k} JR_1^2$. Applying C_3 and C_4 to equation (9) gives:

$$T = T_{R_1} + \frac{1}{4k} JR_1^2 - \frac{1}{4k} Jr^2. \quad (10)$$

At the center of the irradiated area ($r=0$), the temperature, T_C , is given by:

$$T_C = T_{R_1} + \frac{1}{4k} JR_1^2. \quad (11)$$

In our experiments, an electron beam with the acceleration voltage of 300 keV, current density of $J_e=700 \text{ A/m}^2$ and beam size of $2R_1=3 \text{ } \mu\text{m}$ were maintained and they were used in the following calculations. We assume an energy loss of $(dE/dX)=6 \text{ eV}$ per electron, the total energy dissipation in the thin film is given by $\Delta E=J_e \cdot \pi R_1^2 \cdot (dE/dX)=2.04 \times 10^{-8} \text{ W}$ and heat transfer flux density is $J=Q/\pi R_1^2 \cdot h=1.05 \times 10^{11} \text{ W/m}^3$, where a film thickness (h) of 40 nm was used.

The electron beam induced temperature rise and its distribution in a thin film TEM sample is shown in Fig. S4 B and C. Depending on the thermal conductivity of the material, the temperature rise induced by electron beam irradiation can vary significantly. However, for all materials with thermal conductivity larger than $0.1 \text{ W/m}\cdot\text{K}$ (see Table S2), the temperature rise is less than 9 K.

Table S2 Selected materials and their thermal conductivity, k , at room temperature.

Materials	Vacuum	Water vapor (*125°C)	Glycerol	Water	Si ₃ N ₄ (thin film)	Water Ice (*0°C)	Si ₃ N ₄ (bulk)	Si	Au
Thermal conductivity (W/m·K)	0	0.016	0.28	0.58	1.8	2.22	30.1	148	318

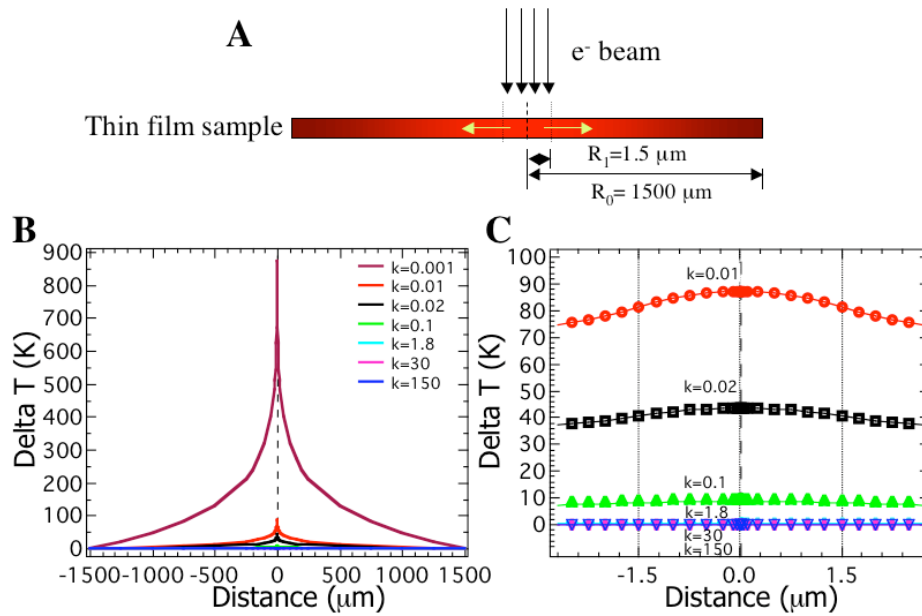


Fig. S4. Temperature rise of the thin film induced by electron beam irradiation. (A) Schematic of a thin film TEM sample with an electron beam irradiated area of radius $1.5 \mu\text{m}$ (cross-section view). (B) Electron beam induced temperature rise and its distribution in the TEM sample. k is thermal conductivity of the film. (C) Enlarged section view of (B).

The temperature rise of the electron beam irradiated area is linearly dependent on the energy loss of the electron beam (Fig. S5).

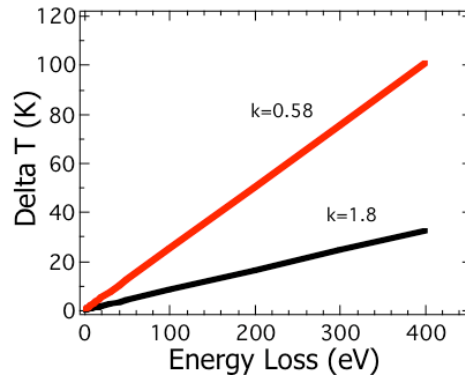


Fig. S5. Temperature rise vs energy loss of the electron beam at the center of irradiated area. An electron beam current of 700 A/m^2 , beam size of $3 \mu\text{m}$ and thin film of Si_3N_4 with $k=1.8 \text{ W/m}\cdot\text{K}$ (black curve) and water with $k=0.58 \text{ W/m}\cdot\text{K}$ (red curve) were used for comparison.

Electron beam induced temperature rise in the liquid cell

The temperature rise of the liquid cell sample under electron beam irradiation can be estimated from the above calculations. From Table S1, we estimate that the total energy loss is no more than 10 eV per electron in the liquid cell configuration as shown in Fig. S6. The temperature rise of the water inside the cell is between 0.8 and 2.5 K, which can be obtained from Fig. S5.

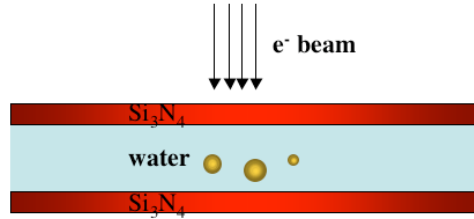


Fig. S6. A schematic of the area of liquid cell under electron beam irradiation (cross-section view). The thickness of each Si_3N_4 membrane is 20 nm and that of the water is 100 nm. Different sized Au nanoparticles (5, 10 and 15nm) are shown for scale.

We further consider different sized gold nanoparticles embedded in the liquid. A uniform temperature distribution inside the particles was assumed. The heat transfer function between the particle and the liquid matrix is given by:

$$A \cdot h \cdot (T_w - T_g) = Q, \quad (12)$$

where A is the particle surface area and $A=4\pi R_g^2$, R_g is the radius of the particle, h is heat transfer coefficient, $h \sim 10^3 \text{ W/m}^2 \cdot \text{K}$, T_w and T_g represent the temperature of the water and the particles, respectively, Q is the total heat induced by the electron beam and $Q=J_e \cdot \pi R_g^2 \cdot (dE/dX)$. Equation (12) becomes

$$(T_w - T_g) = \frac{J_e \cdot (dE/dX)}{4 \cdot h}. \quad (13)$$

Using equation (13), we calculated a temperature rise of $\Delta T=T_w-T_g=0.69 \text{ K}$ for a 15 nm particle and $\Delta T=0.23 \text{ K}$ for a 5 nm particle. Obviously, the difference in the temperature rise between different sized particles is so small that it can be neglected for the particle trajectory analysis.

The ‘‘Mystery’’ of sample temperature rise under electron beam irradiation

Based on our analysis the heating effect from the electron beam irradiation is negligible for most thin film materials. However, there have been many reports on the significant temperature rise induced by electron beam irradiation, for example, melting of the particles under the electron beam^{s4}. Careful examination of those sample configurations reveals that those particles are mostly isolated with only point contact with a supporting carbon film. In this case, the thermal conduction from the particle to the supporting film becomes one-dimensional. At the steady-state, the one-dimensional thermal conduction equation is written as:

$$-k\nabla^2 T(x) = 0. \quad (14)$$

It leads to a temperature distribution:

$$T = C_1 x + C_2. \quad (15)$$

The following boundary conditions are applied. When $x=0$, $C_2=T_{c-film}$ and $dT/dx=C_1=Q/k \cdot \pi r_0^2$, where T_{c-film} is the temperature of the film at the contact, Q is the total heat induced by the energy loss of the electron beam, r_0 is the radius of the contact area perpendicular to h_0 , k is the thermal conductivity of the contact along the distance of h_0 . Substituting C_1 and C_2 into equation (15), we get

$$T = \frac{Q}{k \cdot \pi r_0^2} x + T_{c-film}. \quad (16)$$

The temperature of the particle ($x=h_0$) is given by

$$T_{particle} = \frac{Q \cdot h_0}{k \cdot \pi r_0^2} + T_{c-film}. \quad (17)$$

It is clear that the temperature rise of the particle is dominated by the contact condition between the particle and the film. When there is only point contact, $r_0 \rightarrow 0$, (since the particle is almost totally isolated in vacuum, the thermal conduction could also be very limited, $k \rightarrow 0$), therefore, as $T \rightarrow \infty$ a significant temperature rise is expected.

Conclusions

In conclusion, the electron beam induced temperature rise in water inside the liquid cell is less than 2.5 K in our experiments. The temperature difference between different sized particles embedded in the liquid is negligible. It is noted that the above calculations are an estimation of the maximum induced temperature rise by the electron beam at our experimental settings. Some factors, for example, the liquid vaporization which reduces temperature rise were not considered. It is clear that the temperature rise is negligible for the particle trajectory analysis. The above analysis applies to all the thin film TEM samples.

Under the same electron beam condition, the local temperature rise of a TEM sample can be significant in some cases when the heat conduction is limited. Particle with only point contact with a supporting carbon film, as reported in many cases, is a typical example.

2.2.2 Effects of electron beam on the particle motion

Estimation of the maximum momentum transferable to the nanoparticles

When the high-speed electrons collide with the gold nanoparticles, the momentum of the electrons can directly transfer to the particle and induce particle motion. Here, we examine the maximum momentum transferable to the nanoparticles from the incident electrons and compare it with that from the liquid molecules.

Electron beam contribution

During an elastic collision between an electron and a particle, the maximum energy transferable from the electron to the particle can be estimated by the following equation^{s3,s4}:

$$E_{max} = \frac{2E(E + 2m_e c^2)}{Mc^2}, \quad (18)$$

where $E = m_e c^2 (1/\sqrt{1-\beta^2} - 1)$, m_e and M are the (rest) mass of the electron and the nanoparticle, respectively, c is the speed of light, $\beta=v/c$ and v is the speed of the electron. The maximum momentum, P_e , transferred to the particle from an electron can be calculated by

$$P_e = \sqrt{2ME_{\max}}. \quad (19)$$

The number of incident electrons on the particles can be estimated by $n_e = J_e \cdot \pi r^2$ (in number of electrons $\cdot s^{-1}$), where J_e is the current density of the electron beam, r is the radius of the particle. Since the incident electron beam is perpendicular to the lateral movement of the particles, the effective collisions from the electron beam that contribute to the particles' lateral motion can be estimated by $\sqrt{n_e}$ based on the statistical fluctuations. Therefore, the effective momentum transferred to the particles is estimated by

$$\Delta P_e = P_e \cdot \sqrt{n_e}. \quad (20)$$

Liquid contribution

When a liquid molecule collides elastically with the particle, the maximum transferable energy from the liquid is estimated by

$$E_{\max} = \frac{4m_L ME}{(m_L + M)^2}, \quad (21)$$

where $E=3kT/2$, k is Boltzmann's constant, $T=300$ K is applied, m_L and M are the mass of an liquid molecule and the particle, respectively. The momentum of a liquid molecule transferred to the particle can be estimated by

$$P_L = \sqrt{2ME_{\max}}. \quad (22)$$

The total number of collisions from a liquid molecule per second can be estimated as follows. A collision between a liquid molecule and the gold particle is expected when the liquid molecule moves one molecular distance $2r_L$, where $r_L = (3/4\pi\rho)^{1/3}$ and ρ is the density of the liquid (in number of molecules $\cdot m^{-3}$). The number of collisions of a liquid molecule with the particle is given by $n=v_L/2r_L$ (s^{-1}), where $v_L = \sqrt{3kT/m_L}$ is the velocity of a liquid molecule. The total number of the collisions between the liquid molecules and the particle is given by $N=n \cdot l$, where l is the number of liquid molecules that the gold particle encounters and $l=(4\pi r^2)/(\pi r_L^2)$. The collisions from the liquid molecules are randomly distributed and the net momentum transferred to the particle cancels out. The particle random motion is induced by the statistical fluctuation of the collisions (the effective collisions, $N_{ef} = \sqrt{N}$). Therefore, the effective momentum transferred from the collisions of liquid molecules is estimated by

$$\Delta P^L = P_L \cdot \sqrt{N}. \quad (23)$$

Calculation results

Our calculations show that the maximum momentum transferable from the electron beam to the particle is a few orders of magnitude smaller than that from the liquid, thus should be negligible (see Table S3). The direct momentum transfer from the electron beam to the

particle's lateral motion is four orders of magnitude smaller than that from the liquid and the maximum momentum transfer to the particle vertical motion is two orders of magnitude smaller than liquid contribution. On the concern that the vertical momentum transfer is more significant than the lateral momentum transfer and the vertical momentum can indirectly transfer to the lateral motion by particle rolling, we further quantify the particle motion at different electron beam intensities.

Table S3 Values of mass, speed, density of electrons and liquid molecules and comparison of the maximum momentum transferable to the nanoparticles with different sizes.

	Electron Beam (300 keV)			Liquid (water-15%glycerol)		
Mass (kg)	9.11x10 ⁻³¹ (rest)			4.83x10 ⁻²⁶		
Speed (m·s ⁻¹)	2.328x10 ⁷			5.65x10 ²		
Density	700 A/m ² or 4.37x10 ²¹ electrons/m ² ·s			1.03x10 ³ kg/m ³ or 2.13x10 ²⁸ molecules/m ³		
Total number of collisions (s ⁻¹)	5 nm	10 nm	15 nm	5 nm	10 nm	15 nm
	8.57x10 ⁴	3.43x10 ⁵	7.71x10 ⁵	1.33x10 ¹⁵	5.31x10 ¹⁵	1.19x10 ¹⁶
Effective collisions (s ⁻¹)	2.93x10 ²	5.86x10 ²	8.78x10 ²	1.64x10 ⁷	7.29x10 ⁷	1.09x10 ⁸
Effective transferable momentum (kg·m·s ⁻¹)	1.97x10 ⁻¹⁹	3.94x10 ⁻¹⁹	5.91x10 ⁻¹⁹	1.78x10 ⁻¹⁵	3.57x10 ⁻¹⁵	5.35x10 ⁻¹⁵

Particle motion at different electron beam current densities

We quantify the electron beam effects on the particle motion using a 10 nm particle as a test. Fig. S7A shows trajectories of the particle movement in a liquid thin film under an electron beam current density of 680 A/m² and 160 A/m², respectively. The characteristic behavior of particle motion (small-step movement mixed with large-step jumps) remains unchanged regardless of electron beam intensity (see Fig. S7B). In addition, the diffusion coefficients that are estimated from the linear fits of mean-square-displacement vs time ($\langle x^2 \rangle$ vs t) and $D = \langle x^2 \rangle / 4t$, do not show obvious effects from the change of the electron beam intensity (A significant decrease of diffusion coefficient due to the decrease of electron beam intensity is expected, if the electron beam strongly affects the particle motion.). These experiment results agree with our theoretical calculations.

Conclusions and discussions

We conclude that the electron beam may contribute to the particle motion, but at a rate that is significantly smaller than the thermal component from liquid. Therefore, the effects from the electron beam can be neglected for the current qualitative particle trajectory analysis.

It should be noted that the electron beam effects on the particle motion increases as the beam current density and/or electron energy increases. At significantly high current intensity/energy, the electron beam can direct the particle motion, which is similar to the action of optical tweezers^{s5,s6}. Such an effect is more obvious when a particle is sitting on a curved surface (the momentum transfer from the vertical direction can be visualized),

which has been observed in high temperature molten liquid alloys^{s4}.

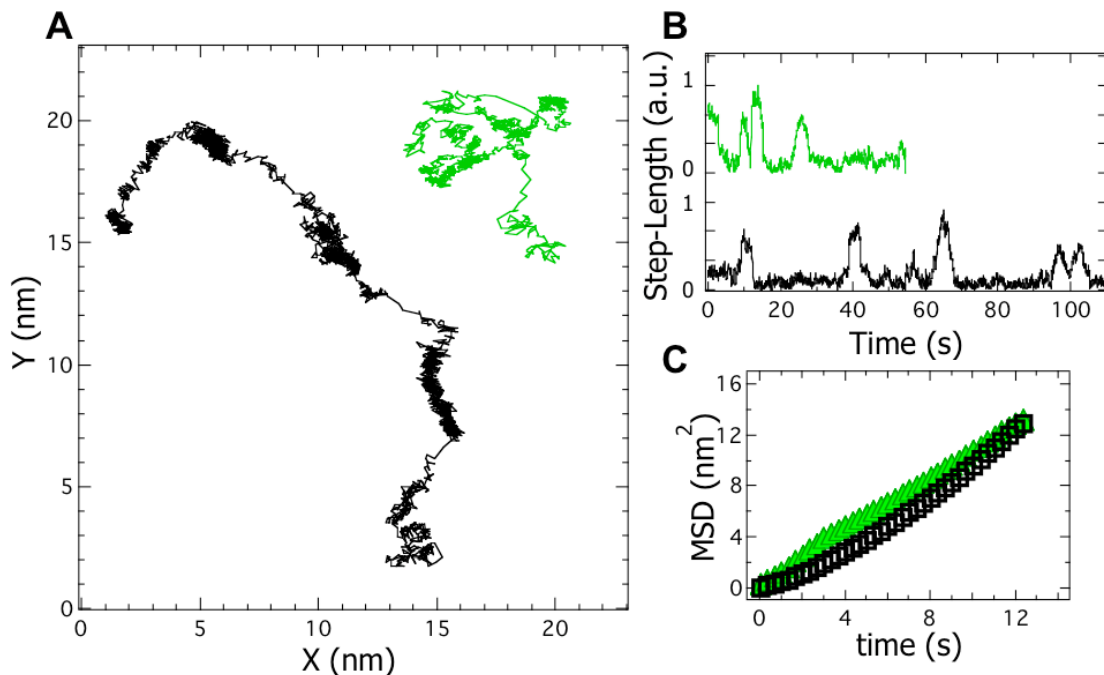


Fig. S7. Motion of a 10 nm particle in a liquid thin film at different electron beam current densities. (A) Trajectories of the particle under an electron beam current density of 680 A/m² (green) and 160 A/m² (black), respectively. (B) Step-length vs time. (C) Mean-square-displacement vs time.

2.2.3 charging effects

We have simulated the trajectory of electrons interacting with a liquid cell sample. The results show that all the electrons penetrate the sample. Direct charge input from the incident electrons is not applied.

The secondary electrons generated by the interaction between the incident electron beam and the sample can be effectively screened by the conductive aqueous solution (a screening distance of 8 nm for the bulk solution).

2.3 Statistical analysis methods on particle displacement vs time In order to quantify the particle movement, we analyzed the particle displacement (λ) during Δt vs time (t). Three methods have been employed here for comparison.

Within the time interval, Δt , we collected N data points corresponding to the particle's center-of-mass positions. Trajectories of the particle motion in (x, y) coordinates are shown in Fig. S8A, with a color gradient indicating the time sequence of movement. In the first method, the displacement (λ) during Δt can be given by the distance from the first point (1) to the last point (N). Therefore,

$$\lambda(t, \Delta t) = \|R_1 - R_N\| = \sqrt{((x(t_i) - x(t_i + \Delta t))^2 + (y(t_i) - y(t_i + \Delta t))^2)}. \quad (24)$$

In the second approach, the displacement (λ) was calculated using the distance between two consecutive averages of N data points,

$$\lambda(t, \Delta t) = \|R_{cm(t_i)} - R_{cm(t_{i+1})}\|. \quad (25)$$

where $R_{cm(t_i)} = (\frac{1}{N} \sum_{i=1}^N x_i, \frac{1}{N} \sum_{i=1}^N y_i)$ is the average of N data points.

In the third approach, the average displacement during Δt was given in terms of the size of the swarm of all data points. The swarm size, $R_G(t; \Delta t)$, can be measured by the following equation:

$$R_G(t; \Delta t) = \frac{1}{N} \sum_{i=1}^N \|R_i(t; \Delta t) - R_{CM}(t; \Delta t)\|, \quad (26)$$

where R_{CM} is the swarm center of mass defined as

$$R_{CM} = \frac{1}{N} \sum_{i=1}^N R_i(t; \Delta t). \quad (27)$$

By taking into account the deviation between the contour length of the particle's real path from 1 to N , $\sum_{i=1}^{N-1} \|R_i - R_{i+1}\|$, and the distance between 1 and N , $\|R_1 - R_N\|$, which is

measured by the ratio $r = \frac{\|R_1 - R_N\|}{\sum_{i=1}^{N-1} \|R_i - R_{i+1}\|}$, we defined particle's displacement, $\lambda(t)$, during

Δt by the following equation

$$\lambda(t) = 2R_G(t; \Delta t) \cdot r. \quad (28)$$

The plots of displacement (λ) vs time (t) during a time interval of 2.33 s using the above three methods are shown in Fig. S8B, C and D. Using the third approach, the characteristics of particle displacement (λ) with the time variable (t), especially the jump diffusion behavior, can be represented explicitly. It should also be noted that the characteristic jump diffusion is not dependent on the time interval that is used for analysis^{S7}. We employed the third method in the manuscript (Figs. 1B and 4B).

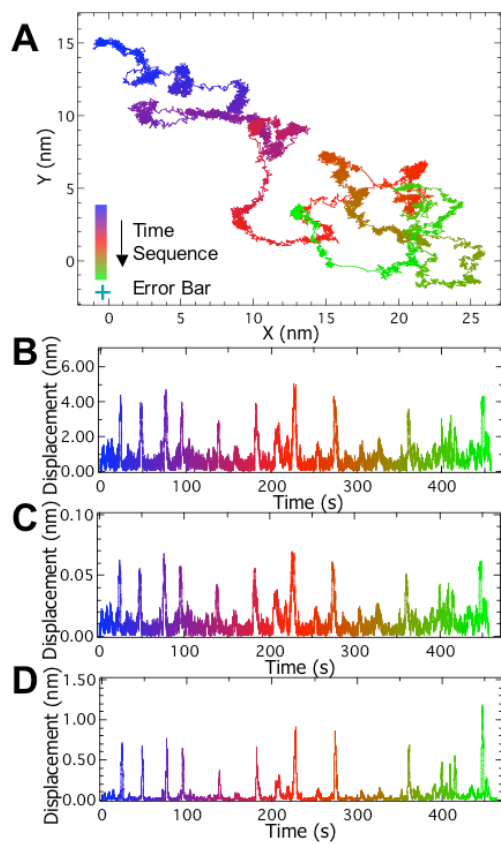


Fig. S8. Comparison of three statistical analysis methods for particle displacement vs time. **(A)** Trajectory of a 5 nm particle movement in a liquid thin film. The time sequence is labeled with a rainbow color scale. **(B)** Displacement during a time interval of 2.33 s vs time as analyzed by method 1. **(C)** Displacement during a time interval of 2.33 s vs time as analyzed by method 2. **(D)** Displacement during a time interval of 2.33 s vs time as analyzed by method 3.

Movie Captions

Movie S1. Diffusion of 5, 10 and 15 nm Au nanoparticles in a liquid thin film.

Movie S2. Diffusion of an asymmetric particle (5x10 nm) in a liquid thin film.

Movie S3. Diffusion of 5 nm particles in a liquid thin film.

In all the movies, time was labeled in the format of hour:minute:second. Sample drift during recording can be calibrated using the drift of a reference particle (a label particle on the nitride membrane without random motion).

References

- S1. Loweth, C. J.; Caldwell, W. B.; Peng, X. G.; Alivisatos, A. P.; Schultz, P. G. *Angew. Chem. Int. Ed.* **1999**, 38, (12), 1808-1812.
- S2. Chen, C. T.; Tseng, F. G.; Chieng, C. C. *Sens. Actuators A: Phys.* **2006**, 130, 12-19.
- S3. *Introduction to analytical electron microscopy* ed. by Hren, J. J.; Goldstein, J. I.; Joy, D. C., Plenum: New York, 1979, p202 and p437.
- S4. Yokota, T.; Howe, J. M.; Jesser, W. A.; Murayama, M. *J. Appl. Phys.* **2004**, 95, (10), 5756-5761.
- S5. Ashkin, A.; Dziedzic, J. M.; Bjorkholm, J. E.; Chu, S. *Opt. Lett.* **1986**, 11, (5), 288-290.
- S6. Ashkin, A.; Dziedzic, J. M. *Science* **1987**, 235, (4795), 1517-1520.
- S7. Raptis, T. E.; Raptis, V. E.; Samios, J. *J. Phys. Chem. B* **2007**, 111, (49), 13683-13693.